PHYSICAL REVIEW B **88**, 085442 (2013)

Fe/CoO(001) and Fe/CoO(111) bilayers: Effect of crystal orientation on the exchange bias

E. Młyńczak,[1,*] B. Matlak,[2] A. Kozioł-Rachwał,[2] J. Gurgul,[1] N. Spiridis,[1] and J. Korecki[1,2]

[1]*Jerzy Haber Institute of Catalysis and Surface Chemistry, Polish Academy of Sciences, Niezapominajek 8, 30-239 Krakow, Poland*

[2]*Faculty of Physics and Applied Computer Science, AGH University of Science and Technology, al. Mickiewicza 30, 30-059 Krakow, Poland*

(Received 17 June 2013; published 30 August 2013)

A comparative study of the structure and magnetism of Fe/CoO(111) and Fe/CoO(001) epitaxial bilayers was performed to investigate the role of uncompensated spins in the exchange bias (EB) phenomenon. Low-energy electron diffraction, x-ray photoelectron spectroscopy, conversion electron Mössbauer spectroscopy (CEMS), and the magneto-optic Kerr effect were used to characterize the structural and magnetic properties of the bilayers. Magnetically compensated and uncompensated CoO films were prepared using molecular beam epitaxy through the evaporation of single Co atomic layers and their subsequent oxidation (layer-by-layer technique) on MgO crystals with (001) and (111) orientations. Two-monolayer-thick ^{57}Fe probes located on top of the oxide films and covered with ^{56}Fe allowed for an analysis of the interfacial chemical and magnetic structure using CEMS. For both structures, submonolayer oxidation of the iron detected at the Fe/CoO interface was found to be accompanied by the formation of a mixed FeCo region. The Fe layers showed fourfold magnetocrystalline anisotropy when grown on CoO(001) and weak uniaxial anisotropy when grown on CoO(111). Although the structural quality and composition of the two structures were comparable, they exhibited distinct EB properties. A hysteresis loop shift as high as 354 Oe at 80 K was obtained for the Fe/CoO(111) bilayer, compared to only 37 Oe for the magnetically compensated Fe/CoO(001).

DOI: 10.1103/PhysRevB.88.085442 PACS number(s): 75.70.Cn, 75.30.Gw, 68.35.Dv

I. INTRODUCTION

Ferromagnetic-antiferromagnetic- (FM-AFM) layered structures have been extensively studied over the last decades[1,2] due to the effect of the exchange bias (EB), which renders these structures technologically important[3,4] and interesting from the viewpoint of basic research.[5] EB occurs as a horizontal shift and broadening of the FM hysteresis loop. One of the most discussed and still controversial aspects of EB is the role of the interfacial spin structure. In the work of Meiklejohn and Bean,[6] the AFM spins at the interface of the FM layer were assumed to be magnetically uncompensated. In that case, the net magnetic moment, which exists in the AFM component of the interface, pins the magnetization direction of the FM component due to a high AFM anisotropy and produces a loop shift. However, the hysteresis loop shifts calculated based on the model of Meiklejohn and Bean are a few orders of magnitude larger than those observed experimentally.[5] Furthermore, an EB was also observed for nominally compensated AFM surfaces, such as CoO(001)[7] and NiO(001).[8] To explain this result, a different approach is needed. The model of Malozemoff[9] considered random roughness at the interface, which produced uncompensated areas for the nominally compensated AFM surface. Schulthess and Butler[10] also noted that for structures with a perfectly compensated AFM order, additional factors, e.g., interfacial defects, are necessary to produce a loop shift. Using element-specific x-ray magnetic circular dichroism, Ohldag *et al.*[11] found uncompensated Ni spins at a nominally compensated Co/NiO(001) interface, localized in the interfacial $CoNiO_x$ layer, which was formed as a result of the oxidation-reduction reactions. The presence of the uncompensated spins resulted in increased coercivity; however, these spins were not sufficient to produce an EB.[11] For the loop shift to be observed, some of the uncompensated spins must be pinned; however, as little as 4% of a monolayer (ML) is sufficient.[12]

Epitaxial FM-AFM bilayers, with CoO as the AFM layer, are well suited for model investigations. CoO has an easily accessible Néel temperature (T_N = 293 K for bulk) and a high magnetocrystalline anisotropy, which enhances the EB effect.[13,14] Furthermore, CoO has a NaCl-type crystal structure to which the AFM order is closely related, which is crucial for the present study. In bulk CoO, the magnetic moments of the Co atoms in a (111) plane are aligned parallel, while the adjacent planes are coupled antiparallel.[15] As a consequence, it is possible to access two different interfacial spin configurations of CoO simply by using CoO(001)- or CoO(111)-oriented layers [Figs. 1(a) and 1(b), respectively]. While CoO(001) atomic layers are compensated in terms of the net magnetic moment, the CoO(111) surface is magnetically uncompensated. In parallel, in contrast to the neutral (001) surface, the (111) surface of the rocksalt oxides is polar, due to the alternatively stacked anionic and cationic layers, as shown in Figs. 1(e) and 1(f). The resulting divergence of the electrostatic energy must be neutralized in such systems to stabilize the surface. Deviations from the stoichiometry, surface reconstructions, or the adsorption of foreign species are possible stabilization mechanisms.[16]

Direct comparisons between bilayer systems with compensated and uncompensated CoO surfaces have been performed; however, contradictory results have been obtained. For CoO/Py epitaxial bilayers, Gökemeijer *et al.*[17] showed that an EB occurred only for the CoO(111) orientation, in contrast to CoO(001). However, Ghadimi *et al.*[18] reported a larger EB effect for $Co/Co_{1-y}O(001)$ in comparison to $Co/Co_{1-y}O$ (111). For Fe_3O_4/CoO epitaxial bilayers, van der Zaag *et al.*[19] found no significant differences in the EB between the (001) and (111) orientations. Thus, it appears that not only the orientation but also the degree of structural perfection plays a role in these systems. To firmly establish the role of the (un)compensation, care must be taken to compare systems that

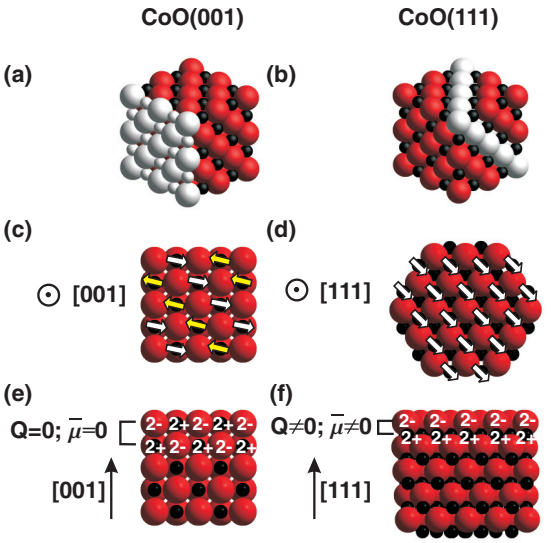

FIG. 1. (Color online) CoO(001) (a) and CoO(111) (b) planes of the bulk NaCl crystal structure, marked by white balls. The red and black balls mark the oxygen and cobalt atoms, respectively. The corresponding arrangement of the magnetic moments (arrows) in the CoO(001) plane (c) and CoO(111) plane (d). Charge arrangement perpendicular to the CoO(001) plane (e) and CoO(111) plane (f). Along the [001] direction, each (001) bilayer is charge-compensated ($Q = 0$) and has no dipole electric moment ($\mu = 0$), while nonzero dipole electric moments along the [111] direction lead to a diverging electrostatic potential, which destabilizes the surface.

are similar with respect to the crystal quality, stoichiometry, and chemical structure of the interfaces.

In the present work, to prepare cobalt oxide layers of both orientations, we used a layer-by-layer method that was previously shown to result in stable polar thin films of FeO grown on MgO(111).[20] By growing bilayer CoO-Fe structures based on magnetically compensated CoO(001) and magnetically uncompensated CoO(111) under precisely controlled conditions and by performing a thorough analysis of the chemical structure of the CoO layers and the Fe/CoO interfaces, we can investigate the relation between the occurrence and magnitude of the EB and the (un)compensation of the AFM interface.

II. EXPERIMENTAL PROCEDURE

Fe/CoO bilayers were prepared in an ultrahigh vacuum (UHV) system equipped with a molecular beam epitaxy facility, following standard surface characterization techniques. Polished MgO(001) and MgO(111) single crystals were used as the substrates. MgO has the same rock salt crystalline structure as CoO, and the mismatch between the two materials is approximately 1%.[21] Metals (Co and Fe) were evaporated from thermally heated BeO crucibles, and MgO layers, used as buffer and capping layers, were evaporated from an MgO piece using an electron beam evaporator. The thickness was controlled by a precisely calibrated quartz crystal monitor.

The substrates were degassed under UHV conditions and annealed at 600 °C for 30 min. Auger electron spectroscopy (AES) was performed on the annealed substrates and showed significant carbon contamination; therefore, a homoepitaxial MgO layer (30 Å thick) was deposited onto the substrates at 450 °C to obtain clean surfaces. The homoepitaxial buffer layers were subsequently annealed at 600 °C for 30 min at an oxygen background pressure of 5×10^{-9} mbar. CoO films were prepared via a layer-by-layer oxidation process of metallic Co MLs. Single layers of metallic Co were deposited at room temperature (RT). The thicknesses of the Co layers corresponded to the Co amount in a single ML of CoO, i.e., 1.19 and 1.39 Å for the (001) and (111) orientation, respectively. The single metallic Co layers were oxidized by exposure to 20 L of molecular oxygen at a partial pressure of $p_{O2} = 5 \times 10^{-8}$ mbar at 270 °C, followed by UHV annealing at 550 °C for 30 min. This procedure ensured a precise control of the oxygen dose for a single metal layer. The crystalline structure of the growing CoO layers was monitored using low-energy electron diffraction (LEED) after each metallic layer deposition and each UHV annealing step. The procedure was repeated ten times for the (001) orientation and nine times for the (111) orientation, resulting in 20-Å-thick CoO films.

After preparation, the CoO layers were transferred to another UHV system using a vacuum suitcase for x-ray photoelectron spectroscopy (XPS) measurements. The XPS spectra were measured using an Al $K\alpha$ (1486.6 eV) x-ray source and an SES R4000 hemispherical analyzer (Gammadata Scienta). The spectra were calibrated using the C 1*s* line at a binding energy of 285 eV. The spectral analysis was conducted with commercial software.[22]

Next, 50-Å-thick Fe layers were deposited onto the CoO films at RT. To characterize the chemical and magnetic structure of the Fe/CoO interface using conversion electron Mössbauer spectroscopy (CEMS), first, an ultrathin (2 ML = 2.86 Å) ^{57}Fe layer was evaporated on the CoO, followed by 33 ML (47 Å) of ^{56}Fe. The samples were capped with approximately 70 Å of MgO. A schematic representation of the samples is shown in Fig. 2.

Magnetic characterization of the samples was performed *ex situ* using the longitudinal magneto-optic Kerr effect (MOKE). Measurements as a function of the azimuthal angle φ between the magnetic field and the characteristic in-plane crystallographic directions were acquired at RT, enabling an identification of the intrinsic magnetic anisotropies in the Fe film. The Fe-CoO magnetic exchange coupling was investigated using the field cooling (FC) procedure. During FC, the samples were placed in a cryostat, where they were cooled from RT passing through the Néel temperature of bulk CoO (291 K) and reaching 80 K in the presence of a static magnetic

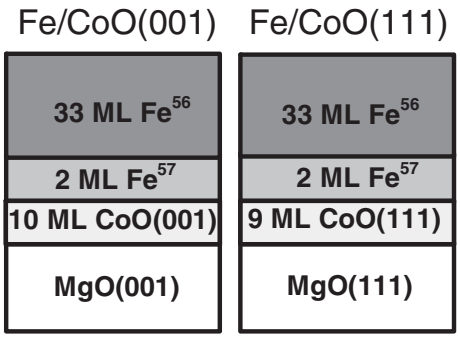

FIG. 2. Schematic representation of the samples.

field of 4000 Oe, oriented along the easiest magnetization direction. Then, the hysteresis loops were measured as a function of temperature, up to 300 K. The exchange coupling was described using the EB field $H_{EB} = (|H_{C1}| - |H_{C2}|)/2$ and the coercive field $H_C = (|H_{C1}| + |H_{C2}|)/2$, where H_{C1} and H_{C2} are the coercive fields of the ascending and descending branches of the hysteresis loop, respectively.

To examine the chemical structure of the Fe/CoO interfaces, CEMS measurements were performed *ex situ* using a standard Mössbauer spectrometer equipped with a He/CH_4 flow proportional detector and a 100-mCi $^{57}Co/Rh$ source. The CEMS spectra were collected under a normal incidence geometry. Commercial software[23] was used to fit the spectra using a Voigt-line-based least-squares method, thus approximating the distribution of the hyperfine magnetic field B_{hf} at a given site with a sum of Gaussian components.

III. RESULTS AND DISCUSSION

A. Chemical and structural characterization

The AES results for the MgO(001) and MgO(111) substrates revealed significant contamination (Fig. 3), including carbon and calcium. To reduce surface contamination, homoepitaxial MgO buffer layers were deposited onto the substrates prior to the preparation of the CoO films. The decreased intensity of the AES C *KLL* (270 eV) and Ca *KLL* (291 eV) lines with respect to the O *KLL* signal (503 eV) indicate that the intrinsic MgO contaminants were covered by the buffer layers.

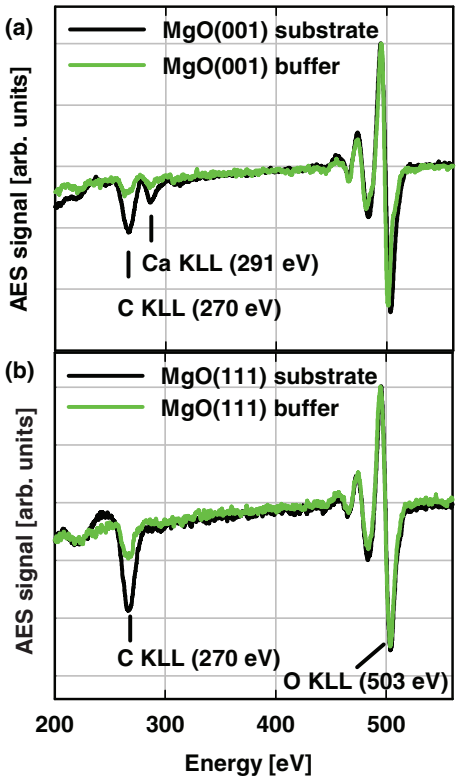

FIG. 3. (Color online) AES spectra of the MgO(001) (a) and MgO(111) (b) substrates and the homoepitaxial buffer layers. The spectra are normalized to the oxygen peak.

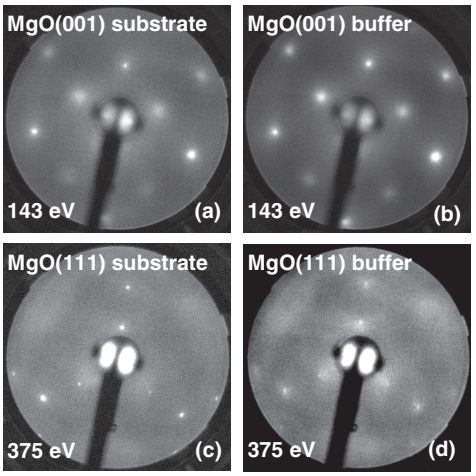

FIG. 4. LEED patterns of the MgO(001) and MgO(111) substrates [(a) and (c), respectively] and of the corresponding homoepitaxial buffer layers deposited onto the substrates [(b) and (d), respectively].

The LEED patterns observed for the substrates and buffers of both orientations verified epitaxial growth of the buffer layers (Fig. 4). As expected, the crystalline symmetry was fourfold for MgO(001) and threefold for MgO(111). For MgO(111), the LEED pattern for $E_P = 375$ eV is shown; for the lower primary beam energies, the spots were faint and the background was high due to charging effects.

LEED was also used to monitor the crystalline quality of the CoO films grown on MgO(001) and MgO(111). The LEED patterns were recorded after each preparation step. Selected patterns are shown in Fig. 5. For both crystal orientations, LEED observations were difficult due to charging effects. The minimum primary beam energy (E_{min}) for which the diffraction pattern was experimentally observable increased with increasing CoO thickness, from 205 eV for 1 ML to 410 eV for 10 ML for CoO grown on MgO(001) [Figs. 5(a) and 5(d)] and from 120 eV for 1 ML to approximately 370 eV for 9 ML for CoO grown on MgO(111) [Figs. 5(e) and 5(h)]. The enhanced charging might be related to the different band gaps of MgO and CoO, which equal 7.8 eV (Ref. 24) and approximately 3 eV,[25] respectively. The patterns observed throughout the entire growth of the CoO films reflect the symmetry of the MgO substrates, and hence, the CoO films that resulted from the layer-by-layer deposition onto the MgO(001) and MgO(111) substrates were unambiguously identified as CoO(001) and CoO(111), respectively.

The diffraction spots observed for CoO(111) were more diffused than those for CoO(001). However, in contrast to CoO(001), where the spots were equally sharp for the metallic and oxidic layers, the differences between the qualities of the images were significant for the CoO(111) case. Due to the enhanced conductivity of the metal surface, the background was suppressed, and the diffraction spots became sharper and brighter after deposition of the metallic Co layer. This finding indicates that the wider and more diffused spots observed for the oxidized layers are related to charging effects rather than being caused by a lower structural quality. For both cases, after each deposition of metallic Co, a LEED pattern was obtained for an E_{min} of approximately 100 eV.

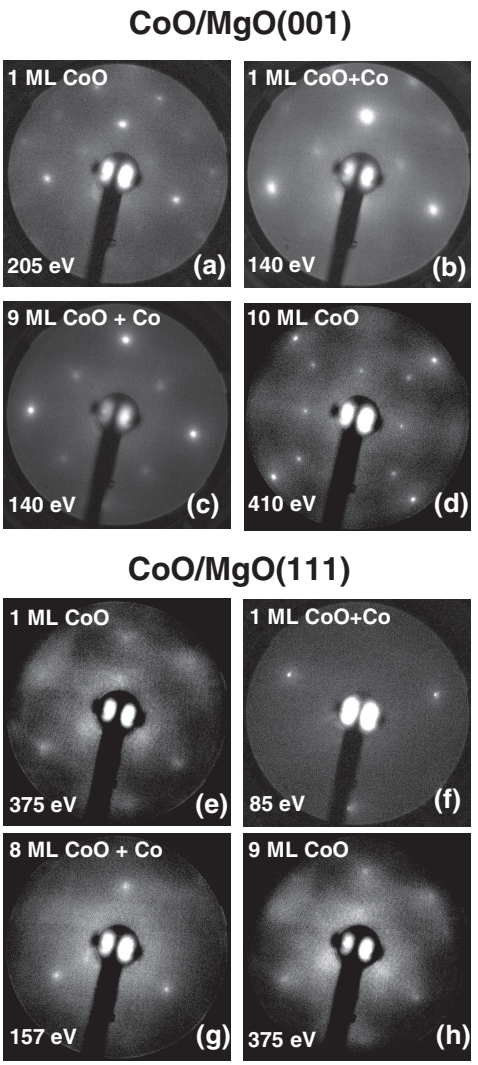

FIG. 5. LEED patterns recorded during CoO layer preparation onto MgO(001) and MgO(111) [(a)–(d) and (e)–(h), respectively].

Charging of the samples influenced the LEED patterns of the Fe films deposited onto CoO(001) and CoO(111). Although the patterns were very weak, with the diffused spots appearing only at high primary beam energies (larger than 300 eV; Fig. 6), the known epitaxial relation with CoO(001), i.e., Fe(001)[110]‖CoO(001)[100],[26] is evident [Fig. 6(a)]. Fe grown on CoO(111) showed a diffused diffraction pattern, in which a sixfold symmetry is clearly visible [Fig. 6(b)], corresponding to the expected epitaxial growth.[27] When Fe is grown

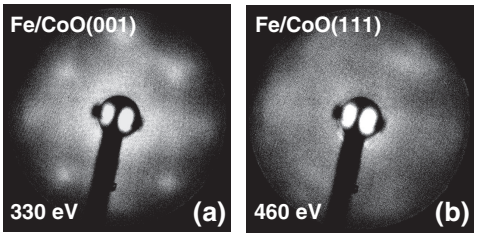

FIG. 6. LEED patterns recorded at the surfaces of Fe grown on CoO(001) (a) and CoO(111) (b).

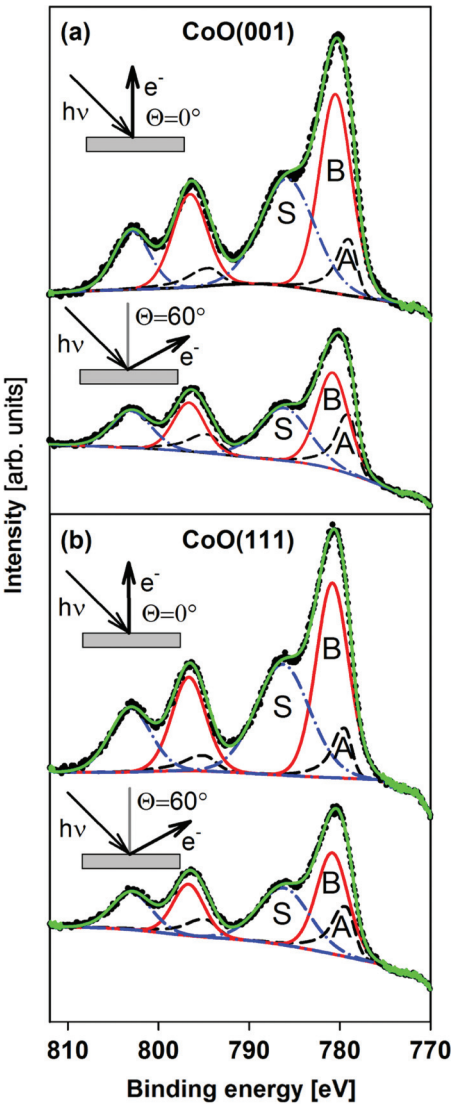

FIG. 7. (Color online) Co $2p$ XPS lines measured for CoO(001) (a) and CoO(111) (b) with $\theta = 0^\circ$ and $\theta = 60^\circ$.

on CoO(111), (110)-oriented grains are formed, which, due to their twofold symmetry, have different in-plane orientations rotated by 120° (Ref. 27). The incoherent superposition of the diffraction patterns from different epitaxial grains leads to the observed pattern of the threefold symmetry, which may be further blurred by charging effects.

XPS was employed to characterize the chemical structure of the CoO films. The spectra recorded at the electron exit angle $\theta = 0^\circ$ (along the surface normal) and at $\theta = 60^\circ$ are presented in Fig. 7. The Co $2p$ lines showed a distinct satellite structure, characteristic of CoO.[28–30] The spectra measured for both CoO(001) and CoO(111) were fitted with two doublets (A and B), accompanied by the satellites (S). All three components contain Co $2p_{3/2}$ and Co $2p_{1/2}$ peaks, located at lower and higher binding energies, respectively. The main parameters of the fitted components are presented in Table I.

A deconvolution of the Co $2p$ spectra showed dominating components at similar binding energies of 780.5 and 780.8 eV for CoO(001) and CoO(111), respectively. The value of 780.5 eV is typical for CoO.[29,31,32] Other parameters, such

TABLE I. The main parameters of the XPS components derived from the Co $2p$ spectra. The binding energy of the Co $2p_{3/2}$ line and the corresponding FWHM are listed in columns three and four. Δ represents the spin-orbit splitting. The percent of the spectral area of a given line is listed in column 6.

Sample	Cp	E_B Co $2p_{3/2}$ (eV)	FWHM (eV)	Δ (eV)	Area (%)
CoO(001)	*A*	778.9	1.9	15.5	17
$\theta = 0°$	*B*	780.5	4.2	16.0	83
	S	785.7	7.0	17.2	–
CoO(001)	*A*	779.0	1.9	15.5	31
$\theta = 60°$	*B*	780.8	4.1	15.8	69
	S	786.1	6.5	16.8	–
CoO(111)	*A*	779.5	1.9	15.4	15
$\theta = 0°$	*B*	780.8	4.2	15.8	85
	S	786.3	7.0	16.8	–
CoO(111)	*A*	779.2	2.0	15.5	26
$\theta = 60°$	*B*	780.8	3.9	15.9	74
	S	786.1	6.5	16.9	–

as spin-orbit splitting, equal to 15.7 and 15.8 eV for CoO(001) and CoO(111), respectively, and the separation between the $2p_{3/2}$ main line (B) and the satellite (S) [5.2 and 5.5 eV for CoO(001) and CoO(111), respectively], agree with the values reported for CoO powder and differ significantly from the values reported for Co_3O_4.[31] In addition, the width of component B, which equals 4.2 eV in both cases, is only slightly larger than the full width at half-maximum (FWHM) reported for CoO powder (3.7 eV). This slight broadening can be easily understood by considering that the binding energy of the cobalt core electrons may be slightly different at the MgO/CoO interface, the CoO surface and the center of the film. In addition to the main doublet B, additional components at the lower binding energy were fitted (doublet A). Their binding energies, equal to 778.9 and 779.4 eV for CoO(001) and CoO(111), respectively, lie between the values expected for metallic Co (778.2 eV) and Co_3O_4 (779.6–779.8 eV).[32,33] The relative intensity of doublet A increases with the angle θ, suggesting that the species responsible for this component are located in the surface region. We identified this component as reduced cobalt oxide, based on the result that the best fit was obtained using an asymmetric peak shape and without additional satellite lines, both characteristic traits of metallic species. In addition, the preparation conditions in our experiment were reducing (each oxidation was followed by annealing); thus, an oxygen deficiency in the surface region is not surprising. In summary, the two CoO films were found to have very similar chemical structures, with the stoichiometry close to Co_1O_1, and slightly reduced surface regions.

Having characterized the composition and crystalline structure of the CoO films, possible stabilization mechanisms of the polar CoO(111) film should be discussed. One possible mechanism is p(2 × 2) octopolar reconstruction, which leads to the formation of {100} nanofacets.[16] This mechanism cannot be excluded due to the vague LEED patterns. The CoO(111) surface might be also stabilized by adsorbed OH^- groups; in that case, the surface is not reconstructed.[34] However, we propose that the CoO(111) film is sufficiently stable due to the metallization of the CoO surface region, and in this case, no additional stabilization mechanisms are needed.

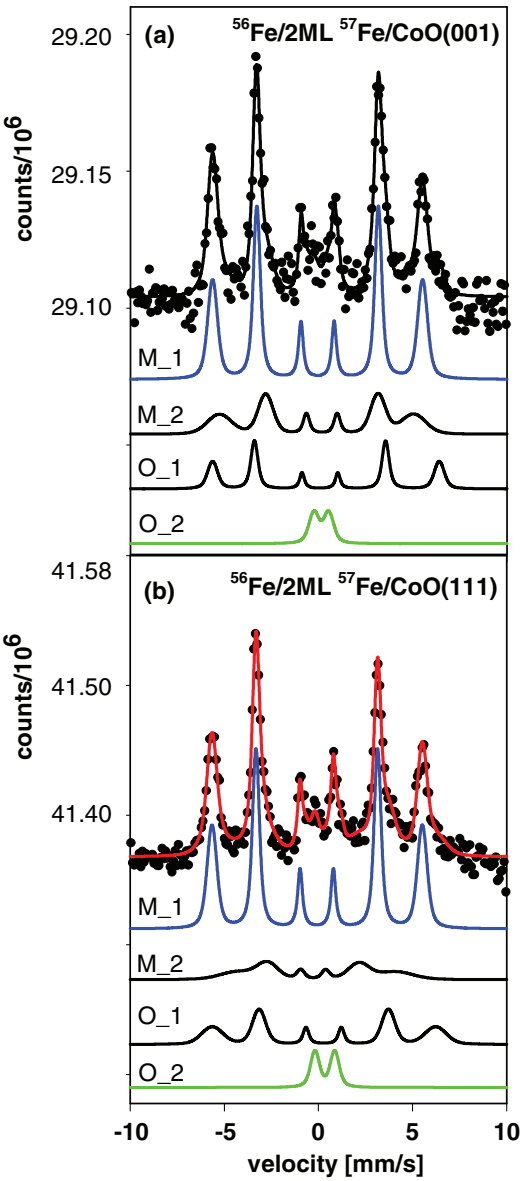

FIG. 8. (Color online) CEMS spectra (dotted line) measured for ^{56}Fe/2 ML ^{57}Fe/CoO(001) (a) and ^{56}Fe/2 ML ^{57}Fe/CoO(111) (b) together with the best fit (solid line), deconvoluted into components, which are shifted along the y axis for clarity.

To investigate the chemical structure of the Fe/CoO interfaces, CEMS spectra were recorded (Fig. 8). The hyperfine parameters, which characterize each spectral component, are given in Table II. Each of the components corresponds to a different atomic site occupied by the ^{57}Fe atoms. Hyperfine parameters are used to identify the chemical state and atomic surroundings of given groups of atoms. The isomer shift (IS), which changes with the density of s electrons at the nucleus, provides information on the oxidation state of the ^{57}Fe atoms, the hyperfine magnetic field (B_{hf}) is related to the magnetic moment of the ^{57}Fe probe atoms and its nearest neighbors, and the quadrupole interaction (ε) is sensitive to the electric field gradient and reflects the local symmetry of the

TABLE II. Hyperfine parameters derived from numerical fits of the CEMS spectra for the Fe/CoO(001) and Fe/CoO(111) interfaces. IS is the average value of the IS with respect to α-Fe. Average quadrupole interaction (ε; sextets) or quadrupole splitting (QS; doublets) are listed in column four. B_{hf} is the average hyperfine magnetic field and ΔB_{hf} is the Gaussian width of the B_{hf} distribution for a given component. RW is the relative weight of the component. The asterisks mark the parameters fixed during the fitting process.

Sample	Site	IS (mm/s)	ε/QS (mm/s)	B_{hf} (T)	ΔB_{hf} (T)	RW (%)
Fe/CoO(001)	M_1	0.04(4)	0.00(2)	34.6(3)	1.2*	55(7)
	M_2	0.1(2)	−0.1(2)	32(2)	3(1)	24(10)
	O_1	0.3(1)	0.1(1)	37(1)	1.2(9)	15(8)
	O_2	0.2(2)	0.8(3)	–	–	6(2)
Fe/CoO(111)	M_1	0.02(1)	0.00(1)	34.6(1)	1.2*	61(4)
	M_2	0.0(4)	0.0(4)	26(3)	5(4)	13(7)
	O_1	0.4(1)	0.0(1)	36.8(8)	3(1)	19(4)
	O_2	0.44(7)	1.0(1)	–	–	7(2)

valence electron charge distribution.[35] The spectra measured for Fe/CoO(001) and Fe/CoO(111) are characterized by a similar set of the components. Therefore, the interfacial model proposed here applies to the bilayers of both orientations, with small differences, which are highlighted below.

Knowing the thickness of the ^{57}Fe probe, it is possible to calculate the amount of ^{57}Fe atoms corresponding to each component using its relative weight (RW). An easily distinguishable component is a doublet (component O_2), which in both spectra comes from a small amount of ^{57}Fe atoms (6–7% of the probe) that diffused into the CoO[36] and which are magnetically decoupled from the rest of the Fe film. The most intense component in both spectra (M_1) is characterized by an IS, indicating its metallic character (IS $\approx$ 0). However, the hyperfine magnetic field, equal to 34.6 T in both spectra, is larger than the typical value for α-Fe (B_{hf} = 33 T at RT).[35] Such an increased B_{hf} is a result of the proximity of Co atoms to Fe atoms at the Fe-CoO interface. Because the XPS measurements indicated that the surfaces of the CoO films were reduced, we interpret component M_1 as originating from the metallic intermixed Fe-Co interfacial region. In iron-rich FeCo alloys, the hyperfine magnetic field at the Fe nucleus increases almost linearly with the Co content, reaching 35 T for 10 at.% of Co, i.e., $Fe_{0.9}Co_{0.1}$.[37] Additional CEMS measurements conducted with a thicker probe layer (not shown) revealed that approximately 4 Å of iron is mixed with cobalt at the Fe/CoO interface.

Between the two remaining components in the spectra, one has a metallic (M_2) and one has an (O_1) oxidic character. The O_1 component, with a hyperfine magnetic field of B_{hf} = 37 T, is characterized by an IS = 0.3–0.4 mm/s, which is typical for bulk iron in the Fe^{3+} oxidation state.[35] The oxidation of Fe atoms is a result of the CoO proximity and often accompanies the formation of a metallic alloy at the metal/oxide interface.[38] The hyperfine magnetic field of the O_1 component is significantly lower than expected for different Fe_2O_3 phases (approximately 50 T)[35] but is close to the value of 38.4 T reported for α-FeOOH.[39] However, the identification of the O_1 component in terms of stoichiometric bulk phases may not be relevant due to the low-dimensional nature of the interfacial iron oxide. Hence, we interpret the interfacial oxidation in the Fe/CoO bilayers as the formation of iron-oxygen bonds, most likely due to the incorporation of oxygen atoms in the hollow sites of the bcc Fe structure, analogous to Fe/MgO.[40] The metallic component M_2, identified by an IS close to zero, exhibited a markedly different hyperfine magnetic field for the (001) and (111) orientations: B_{hf} = 32 T and B_{hf} = 26 T, respectively. In combination with the large width of the B_{hf} distribution, this finding indicates an interfacial origin of this component. Apparently, at the Fe/CoO(001) interface, the coordination of the Fe atoms to their metallic neighbors is different than at the more defective Fe/CoO(111) interface. A similar high sensitivity of the hyperfine magnetic field to the local atomic coordination was recently demonstrated for the Fe/MgO interface.[40] The amount of iron oxide formed at the Fe/CoO interface corresponds to only a fraction of the ML.

If we assume that only components O_1 and M_2 come from the interface, while the FeCo mixed region links this interfacial layer with the interior of the Fe film, the quantitative considerations lead to the conclusion that the ^{57}Fe grown on CoO formed islands, which is in line with recent experimental findings.[41] Consequently, the amount of iron oxide was recalculated to 40% of the interfacial Fe ML for Fe/CoO(001) and to 60% for Fe/CoO(111). This result is similar to the finding of 0.3 ML of FeO based on x-ray absorption spectroscopy at the interface with CoO in an Fe/CoO/Ag(001) structure.[42] The small difference in the amount of the interfacial iron oxide for Fe/CoO(001) and Fe/CoO(111) may be related to different terminations of the CoO surfaces and thus different oxidation conditions.

In summary, the Fe/CoO(001) and Fe/CoO(111) bilayers were very similar in terms of the crystalline quality and stoichiometry of the CoO films, as well as in the chemical structure of the Fe/CoO interface.

B. Magnetic properties

The MOKE measured at RT for different azimuthal angles φ revealed the intrinsic magnetic anisotropies of the two structures. The angle φ was measured with respect to MgO[100] and MgO[−110] for Fe/CoO/MgO(001) and Fe/CoO/MgO(111), respectively. Representative hysteresis loops are shown in Fig. 9(a), while Fig. 9(b) presents polar plots of the reduced remanence. For both orientations, the coercivity measured along the easiest anisotropy direction was equal to 12 Oe. Significant differences appeared in the saturation field (H_S) along the hardest anisotropy directions, which indicates differences in the effective magnetic anisotropies. For Fe/CoO(001), H_S equals 500 Oe. Using the bulk magnetization for the Fe layer, this value corresponds to an effective anisotropy of 4.2×10^5 ergs/cm^3, which is very close to the magnetocrystalline anisotropy of bulk Fe (4.8×10^5 ergs/cm^3; Ref. 43). Meanwhile, for Fe/CoO(111), H_S = 100 Oe, which reflects a much smaller value for the effective anisotropy, i.e., 0.84×10^5 ergs/cm^3.

Fe grown on CoO(001) exhibited two orthogonal in-plane easy axes, along the Fe[100] and Fe[010] directions, as expected for Fe(001) films. In contrast, the magnetic anisotropy

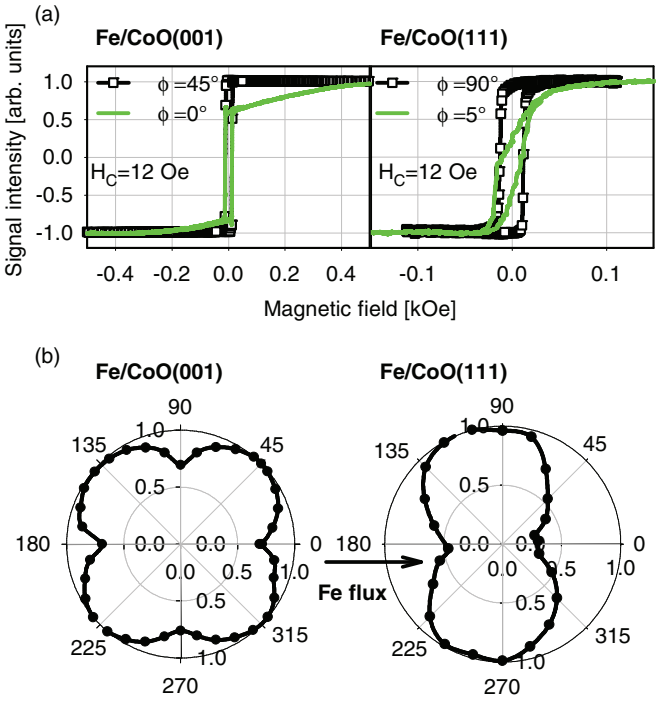

FIG. 9. (Color online) (a) Hysteresis loops measured at RT along the easiest and hardest anisotropy directions, corresponding to $\varphi = 45^\circ$ and $\varphi = 0^\circ$ for Fe/CoO(001) and $\varphi = 90^\circ$ and $\varphi = 5^\circ$ for Fe/CoO(111). The azimuthal angle is measured relative to the MgO[100] and MgO[−110] directions for Fe/CoO(001) and Fe/CoO(111), respectively. (b) Polar plots of the reduced remanence showing the fourfold anisotropy of Fe/CoO(001) and the uniaxial anisotropy of Fe/CoO(111).

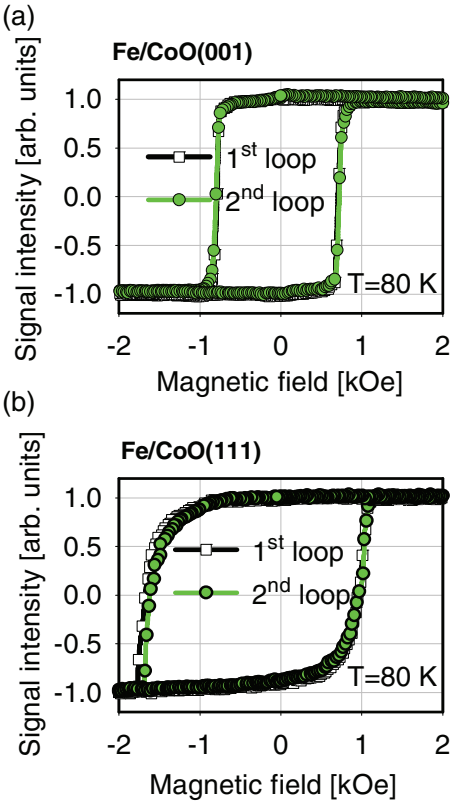

FIG. 10. (Color online) First and second hysteresis loops measured at 80 K after FC for Fe/CoO(001) (a) and Fe/CoO(111) (b).

of the Fe film grown on CoO(111) was uniaxial. Indeed, the Fe(110) surface contains only one easy magnetocrystalline anisotropy axis (Fe[100]), but the uniaxial magnetic anisotropy (UMA) presently observed for Fe/CoO(111) cannot be of magnetocrystalline origin because the Fe film is composed of grains rotated by 120°. The uniaxial anisotropy contributions may have diverse origins: interface anisotropy, as in Fe/GaAs(100),[44] shape anisotropy,[45] or growth-induced anisotropy, which originates from the shadowing effect.[46,47] Although the evaporator used in this study produced an Fe flux at only 12° from the substrate normal, growth-induced anisotropy[46] was responsible for the UMA in the Fe/CoO(111) sample. The easy magnetization direction was oriented perpendicular to the projection of the Fe flux direction onto the sample surface, which was also verified in analogous samples prepared on substrates rotated relative to the evaporator. The UMA contribution is not apparent for the Fe/CoO(001) sample; for that case, the total magnetic anisotropy is dominated by the magnetocrystalline term.

To investigate the AFM-FM magnetic exchange couplings that are characteristic of Fe/CoO(001) and Fe/CoO(111), the samples were field cooled to 80 K. The cooling magnetic field was applied along the easiest magnetization directions because the hysteresis loops before FC were very similar in this case. At 80 K, both systems showed a large coercivity, which increased by factors of 60 (up to $H_C = 740$ Oe) and 100 (up to $H_C =$ 1280 Oe) relative to RT for Fe/CoO(001) and Fe/CoO(111), respectively (Fig. 10).

The coercivity in AFM-FM systems is known to follow the number of uncompensated AFM interfacial spins,[11] the majority of which are rotatable.[12] However, Radu *et al.* argued that the spins belonging to the AFM layer might be rotatable only when the interfacial region has a lowered AFM anisotropy.[48] An interfacial region supplying AFM spins that can rotate together with the FM might exist also for nominally compensated systems as a result of roughness or other structural defects.[48] In our samples, the FM/AFM interface contains mixed FeCo regions, which, for both orientations, may be a source of magnetic moments that increase the coercivity. However, the much larger coercivity enhancement observed for the Fe/CoO(111) system suggests a more complex phenomenon, which is also reflected in the differences in the EB fields, which are clearly shown in Fig. 10. For both configurations, the first hysteresis loop measured at 80 K (first loop) was shifted by $H_{EB} = 37$ Oe and $H_{EB} = 354$ Oe for Fe/CoO(001) and Fe/CoO(111), respectively, in the direction opposite to the magnetic field applied during FC. The value of $H_{EB} = 354$ Oe measured at 80 K is much larger than previously reported values for other bilayer systems based on CoO(111) and a metallic FM layer.[17,18,27,49] The occurrence of the training effect was verified through a subsequent measurement of another hysteresis loop (second loop), which was identical to the first loop for Fe/CoO(001) and indicated a slightly (7%) decreased EB field ($H_{EB} = 328$ Oe) for Fe/CoO(111). This weak training effect is related to the

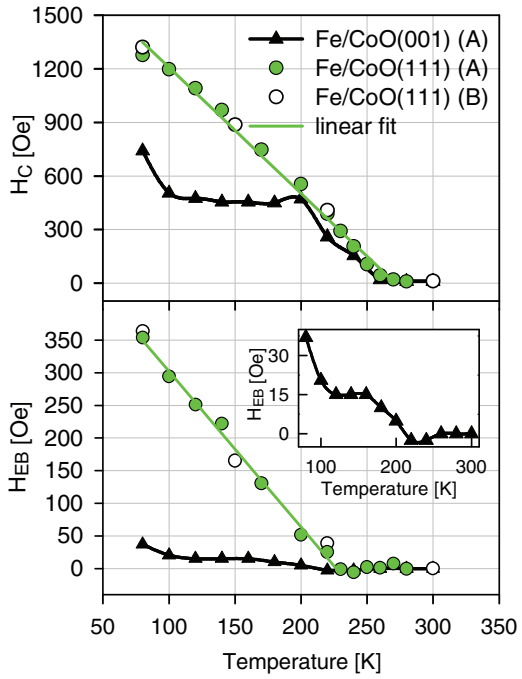

FIG. 11. (Color online) Temperature dependence of the coercive field (H_C) and EB field (H_{EB}) for Fe/CoO(001) and Fe/CoO(111) measured after a single FC procedure (procedure A, full symbols) and measured after FC was performed for Fe/CoO(111) separately at each temperature (procedure B, empty symbols). The inset presents a rescaled H_{EB} temperature dependence for the Fe/CoO(001) sample. For the Fe/CoO(111) sample, both parameters were fitted with a linear temperature dependence. For Fe/CoO(001), the solid lines are guides to the eye.

high structural quality of the bilayers, as this effect is usually observed for polycrystalline samples.[50,51]

The EB effect in the Fe/CoO bilayers was studied as a function of temperature. Hysteresis loops were measured for temperatures ranging from 80 to 300 K after FC to 80 K (procedure A). To account for the slight training effect observed for the Fe/CoO(111) system, measurements were also performed in which the FC was performed to each temperature separately (procedure B). The temperature dependence of H_C and H_{EB} is presented in Fig. 11. Measurement procedures A and B led to very similar results, as expected based on the very small training effect observed for the Fe/CoO(111) sample. For both samples, H_{EB} and H_C decreased with temperature. However, the temperature dependences of H_{EB} and H_C for Fe/CoO(001) and Fe/CoO(111) are different. For Fe/CoO(111), both quantities show a linear temperature dependence; however, a plateau for intermediate temperatures is observed for Fe/CoO(001). For both samples, the coercivity is larger at lower temperatures due to the increased magnetocrystalline anisotropies of both Fe and CoO. The coercivity enhancement is observed below $T = 265$ K, which is slightly lower than the Néel temperature of bulk CoO, as expected.

The linear temperature dependence of H_{EB} found for Fe/CoO(111) has been observed in many EB systems.[14,52,53] According to the Malozemoff EB model,[9] H_{EB} is proportional to the energy stored in the domain wall (σ_{AF}), which is formed in the antiferromagnet. Because $\sigma_{AF} \propto (A_{AFM} K_{AFM})^{1/2}$, where A_{AFM} represents the exchange stiffness and K_{AFM} indicates the anisotropy constant of the AFM component, the temperature dependence of H_{EB} is governed by changes in K_{AFM}, assuming that A_{AFM} is temperature independent. For a cubic AFM anisotropy, the linear temperature dependence of $H_{EB}(T)$ within the Malozzemoff model follows from the temperature dependence of the anisotropy constant: $K_{AFM}(T) = K_{AFM}(0)(1 - T/T_N)^2$ (Refs. 9 and 52). Consequently, the temperature dependence of H_{EB} for Fe/CoO(111) was fitted with $H_{EB}(T) \propto (1 - T/T_B)$, where T_N was replaced by the blocking temperature $T_B = 227$ K. T_B is the temperature above which the AFM domains become stable against the exchange interactions with the FM layer,[49] and H_{EB} vanishes. The blocking temperature found for the Fe/CoO(111) bilayer is lower than the Néel temperature of bulk CoO. Such a significant lowering of T_B with respect to T_N could be attributed to the deviation from the Co_1O_1 stoichiometry towards Co_3O_4 ($T_N(Co_3O_4) = 34$ K)T_N.[27] However, because the CoO films prepared in the present study were reduced rather than over-oxidized (Sec. III A), we propose that the lowered T_B is due to the small thickness of the CoO films (20 Å). Similarly reduced values of T_B have been observed for diverse systems, such as CoNiO/NiFe, NiO/NiFe,[54] and Fe_3O_4/CoO[53] bilayers with AFM layers thinner than approximately 50 Å. This effect is related to the weakening of exchange interactions with decreasing AFM layer thickness rather than a finite size effect of the T_N reduction.[53,55]

The EB field measured for Fe/CoO(001) was much smaller compared to Fe/CoO(111) and presented a more complex temperature dependence. Below 210 K, the hysteresis loop was shifted in the direction opposite to the magnetic field used for FC, which is a typical negative EB effect.[5] After the rapid low-temperature decrease, a plateau region occurred between 120 and 160 K, followed by a linear decrease to 210 K. A similar temperature dependence was reported for the EB in polycrystalline Py/CoO layers, in which the EB followed the thermoremanent magnetization of the CoO interfacial uncompensated spins.[56] The measurements between 220 and 240 K exhibited hysteresis loops slightly shifted along the FC direction, indicating a small positive EB effect. Similar effects near the blocking temperature have been previously reported for polycrystalline Co/CoO[57] and textured CoO/Co(111)[58] bilayers. However, for our sample, this positive H_{EB} equals only 3 Oe, which is on the order of the experimental uncertainty; hence, we find this value negligible. Thus, for the Fe/CoO(001) sample, we consider $T_B = 210$ K as the temperature below which a negative EB occurs. This value is similar to that of Fe/CoO(111), which supports the interpretation of its relation to the reduced thickness of the CoO films.

IV. SUMMARY AND CONCLUSIONS

In conclusion, we have investigated Fe/CoO(001) and Fe/CoO(111) epitaxial bilayers with nominally compensated and uncompensated FM-AFM interfaces through structural and magnetic characterization. The layer-by-layer deposition method employed in this work resulted in nearly stoichiometric CoO films with reduced surfaces. A fraction of a ML of Fe oxide was identified at the Fe/CoO interfaces for both orientations. The Fe oxidation was accompanied by the

formation of a mixed metallic $Fe_{0.9}Co_{0.1}$ region. The Fe films grown on CoO(001) exhibited the expected fourfold magnetic anisotropy, while the Fe films deposited on CoO(111) were uniaxial. FC resulted in a strong coercivity enhancement for both samples, while the EB was drastically larger for Fe/CoO(111) compared to Fe/CoO(001). The temperature dependences of H_{EB} and H_C were similar within each system, yet different for the two crystal orientations.

We attribute the EB bias and coercivity enhancement in the Fe/CoO bilayers to the uncompensated pinned and rotatable spins, respectively, present at the Fe/CoO interface. The number of uncompensated spins is much larger for CoO(111) than for nominally compensated CoO(001), where their only source is the atomic level roughness. Furthermore, the intrinsic magnetic anisotropy of the Fe film grown on CoO(111) is much weaker than in the Fe/CoO(001) configuration; thus, the total anisotropy of the system is much more sensitive to the unidirectional anisotropy introduced during FC. The origin of the remarkably strong EB observed for Fe/CoO(111) should be attributed to the combination of the uncompensated spin structure of CoO(111) and the low intrinsic magnetic anisotropy of the Fe film. Therefore, we provide direct evidence of the dominant role of crystalline orientation in the magnetic behavior of epitaxial systems.

ACKNOWLEDGMENTS

This work was supported in part by the National Science Center (NCN), Poland (Grant No. 2011/02/A/ST3/00150), and by the MPD/2008/3 and TEAM/2008-2/3 projects of the Foundation for Polish Science (FNP) cofinanced by the European Union European Regional Development Fund.

*Author to whom correspondence should be addressed: ncmlyncz@cyf-kr.edu.pl

[1] M. Finazzi, L. Duò, and F. Ciccacci, Surf. Sci. Rep. **64**, 139 (2009).
[2] K. O'Grady, L. E. Fernandez-Outon, and G. Vallejo-Fernandez, J. Magn. Magn. Mater. **322**, 883 (2010).
[3] C. Tsang, R. E. Fontana, T. Lin, D. E. Heim, V. S. Speriosu, B. A. Gurney, and M. L. Williams, IEEE Trans. Magn. **30**, 3801 (1994).
[4] S. S. P. Parkin, K. P. Roche, M. G. Samant, P. M. Rice, R. B. Beyers, R. E. Scheuerlein, E. J. O'Sullivan, S. L. Brown, J. Bucchigano, D. W. Abraham, Yu Lu, M. Rooks, P. L. Trouilloud, R. A. Wanner, and W. J. Gallagher, J. Appl. Phys. **85**, 5828 (1999).
[5] J. Nogués and I. K. Schuller, J. Magn. Magn. Mater. **192**, 203 (1999).
[6] W. H. Meiklejohn and C. P. Bean, Phys. Rev. **102**, 1413 (1956).
[7] J. Gurgul, K. Freindl, A. Kozioł-Rachwał, K. Matlak, N. Spiridis, T. Ślęzak, D. Wilgocka-Ślęzak, and J. Korecki, Surf. Interface Anal. **42**, 696 (2010).
[8] P. Luches, S. Benedetti, A. di Bona, and S. Valeri, Phys. Rev. B **81**, 054431 (2010).
[9] A. P. Malozemoff, Phys. Rev. B **35**, 3679 (1987).
[10] T. C. Schulthess and W. H. Butler, Phys. Rev. Lett. **81**, 4516 (1998).
[11] H. Ohldag, T. J. Regan, J. Stöhr, A. Scholl, F. Nolting, J. Lüning, C. Stamm, S. Anders, and R. L. White, Phys. Rev. Lett. **87**, 247201 (2001).
[12] H. Ohldag, A. Scholl, F. Nolting, E. Arenholz, S. Maat, A. T. Young, M. Carey, and J. Stöhr, Phys. Rev. Lett. **91**, 017203 (2003).
[13] A. E. Berkowitz and K. Takano, J. Magn. Magn. Mater. **200**, 552 (1999).
[14] M. Gruyters, J. Magn. Magn. Mater. **248**, 248 (2002).
[15] W. L. Roth, Phys. Rev. **110**, 1333 (1958).
[16] J. Goniakowski, F. Finocchi, and C. Noguera, Rep. Prog. Phys. **71**, 016501 (2008).
[17] N. J. Gökemeijer, R. L. Penn, D. R. Veblen, and C. L. Chien, Phys. Rev. B **63**, 174422 (2001).
[18] M. R. Ghadimi, B. Beschoten, and G. Güntherodt, Appl. Phys. Lett. **87**, 261903 (2005).
[19] P. J. van der Zaag, A. R. Ball, L. F. Feiner, R. M. Wolf, and P. A. A. van der Heijden, J. Appl. Phys. **79**, 5103 (1996).
[20] J. Gurgul, E. Młyńczak, N. Spiridis, and J. Korecki, Surf. Sci. **606**, 711 (2012).
[21] S. A. Chambers, Surf. Sci. Rep. **39**, 105 (2000).
[22] CasaXPS 2.3.15, Casa Software Ltd., Teignmouth, UK (2009).
[23] K. Lagarec and D. G. Rancourt, Recoil 1.05, Mössbauer Analysis Software for Windows (2002).
[24] D. M. Roessler and W. C. Walker, Phys. Rev. **159**, 733 (1967).
[25] V. I. Anisimov, M. A. Korotin, and E. Z. Kurmaev, J. Phys.: Condens. Matter **2**, 3973 (1990).
[26] A. Brambilla, P. Sessi, M. Cantoni, L. Duò, M. Finazzi, and F. Ciccacci, Thin Solid Films **516**, 7519 (2008).
[27] G. Nowak, A. Remhof, F. Radu, A. Nefedov, H.-W. Becker, and H. Zabel, Phys. Rev. B **75**, 174405 (2007).
[28] K. S. Kim, Phys. Rev. B **11**, 2177 (1975).
[29] G. A. Carson, M. H. Nassir, and M. A. Langell, J. Vac. Sci. Technol. A **14**, 1637 (1996).
[30] S. Valeri, A. Borghi, G. C. Gazzadi, and A. di Bona, Surf. Sci. **423**, 346 (1999).
[31] T. J. Chuang, C. R. Brundle, and D. W. Rice, Surf. Sci. **59**, 413 (1976).
[32] S. C. Petitto and M. A. Langell, J. Vac. Sci. Technol. A **22**, 1690 (2004).
[33] C. R. Brundle, T. J. Chuang, and D. W. Rice, Surf. Sci. **60**, 286 (1976).
[34] D. Cappus, M. Haßel, E. Neuhaus, M. Heber, F. Rohr, and H.-J. Freund, Surf. Sci. **337**, 268 (1995).
[35] N. N. Greenwood and T. C. Gibb, *Mössbauer Spectroscopy* (Chapman and Hall, London, 1971).
[36] V. G. Bhide and G. K. Shenoy, Phys. Rev. **147**, 306 (1966).
[37] E. Jartych, J. K. Zurawicz, and M. Budzyński, J. Phys.: Condens. Matter **5**, 927 (1993).
[38] T. J. Regan, H. Ohldag, C. Stamm, F. Nolting, J. Lüning, J. Stöhr, and R. L. White, Phys. Rev. B **64**, 214422 (2001).
[39] J. B. Forsyth, I. G. Hedley, and C. E. Johnson, J. Phys. C **1**, 179 (1968).
[40] E. Młyńczak, K. Freindl, N. Spiridis, and J. Korecki, J. Appl. Phys. **113**, 024320 (2013).
[41] A. Brambilla, A. Picone, M. Finazzi, L. Duò, and F. Ciccacci, Surf. Sci. **605**, 95 (2011).
[42] R. Abrudan, J. Miguel, M. Bernien, C. Tieg, M. Piantek, J. Kirschner, and W. Kuch, Phys. Rev. B **77**, 014411 (2008).

[43]C. D. Graham, Jr., Phys. Rev. **112**, 1117 (1958).
[44]O. Thomas, Q. Shen, P. Schieffer, N. Tournerie, and B. Lépine, Phys. Rev. Lett. **90**, 017205 (2003).
[45]Q. Zhan, S. Vandezande, C. Van Haesendonck, and K. Temst, Appl. Phys. Lett. **91**, 122510 (2007).
[46]Q. Zhan, C. Van Haesendonck, S. Vandezande, and K. Temst, Appl. Phys. Lett. **94**, 042504 (2009).
[47]S. van Dijken, L. C. Jorritsma, and B. Poelsema, Phys. Rev. Lett. **82**, 4038 (1999).
[48]F. Radu, A. Westphalen, K. Theis-Bröhl, and H. Zabel, J. Phys.: Condens. Matter **18**, L29 (2006).
[49]F. Radu, S. K. Mishra, I. Zizak, A. I. Erko, H. A. Durr, W. Eberhardt, G. Nowak, S. Buschhorn, H. Zabel, K. Zhernenkov, M. Wolff, D. Schmitz, E. Schierle, E. Dudzik, and R. Feyerherm, Phys. Rev. B **79**, 184425 (2009).
[50]A. Hochstrat, Ch. Binek, and W. Kleemann, Phys. Rev. B **66**, 092409 (2002).
[51]C. Fleischmann, F. Almeida, J. Demeter, K. Paredis, A. Teichert, R. Steitz, S. Brems, B. Opperdoes, C. Van Haesendonck, A. Vantomme, and K. Temst, J. Appl. Phys. **107**, 113907 (2010).
[52]Z. Y. Liu and S. Adenwalla, J. Appl. Phys. **94**, 1105 (2003).
[53]P. J. van der Zaag, Y. Ijiri, J. A. Borchers, L. F. Feiner, R. M. Wolf, J. M. Gaines, R. W. Erwin, and M. A. Verheijen, Phys. Rev. Lett. **84**, 6102 (2000).
[54]A. J. Devasahayam and M. H. Kryder, J. Appl. Phys. **85**, 5519 (1999).
[55]X. Y. Lang, W. T. Zheng, and Q. Jiang, Nanotechnology **18**, 155701 (2007).
[56]K. Takano, R. H. Kodama, A. E. Berkowitz, W. Cao, and G. Thomas, Phys. Rev. Lett. **79**, 1130 (1997).
[57]T. Gredig, I. N. Krivorotov, P. Eames, and E. D. Dahlberg, Appl. Phys. Lett. **81**, 1270 (2002).
[58]F. Radu, M. Etzkorn, R. Siebrecht, T. Schmitte, K. Westerholt, and H. Zabel, Phys. Rev. B **67**, 134409 (2003).